ADVANCED FUNCTIONAL MATERIALS

FULL PAPER

DOI: 10.1002/adfm.200500647

The Influence of TiO_2 Particle Size in $TiO_2/CuInS_2$ Nanocomposite Solar Cells**

By *Ryan O'Hayre*,* *Marian Nanu*, *Joop Schoonman*, *Albert Goossens*, *Qing Wang*, and *Michael Grätzel*

The recently developed $CuInS_2/TiO_2$ 3D nanocomposite solar cell employs a three-dimensional, or "bulk", heterojunction to reduce the average minority charge-carrier-transport distance and thus improve device performance compared to a planar configuration. 3D nanocomposite solar-cell performance is strongly influenced by the morphology of the TiO_2 nanoparticulate matrix. To explore the effect of TiO_2 morphology, a series of three nanocomposite solar-cell devices are studied using 9, 50, and 300 nm TiO_2 nanoparticles, respectively. The photovoltaic efficiency increases dramatically with increasing particle size, from 0.2 % for the 9 nm sample to 2.8 % for the 300 nm sample. Performance improvements are attributed primarily to greatly improved charge transport with increasing particle size. Other contributing factors may include increased photon absorption and improved interfacial characteristics in the larger-particle-size matrix.

1. Introduction

In recent years, the desire for low-cost solar cells has lead to the exploration of new photovoltaic designs based on nanostructured materials. Research by Grätzel and O'Regan,[1] Heeger and co-workers,[2] and others[3–5] has produced a variety of successful solar-cell designs using nanometer-scale blends or interpenetrating systems. Recently, we have reported on a new, completely inorganic solar-cell design based on nanostructured n-type TiO_2 and p-type $CuInS_2$ (CIS).[6] In 3D nanostructured TiO_2/CIS solar cells, as in traditional thin-film CIS solar cells, photons are absorbed in the p-type CIS layer and converted into electron–hole pairs. The holes are conducted through the CIS layer to a back-electrode contact, while the electrons must transport to the p–n junction where they are then transferred to the TiO_2. Compared to a planar device, the nanostructured interface between the p-type CIS layer and the n-type TiO_2 matrix shortens the average minority-carrier diffusion length, thereby improving the collection efficiency and providing the device with a higher tolerance to the presence of impurities. TiO_2/CIS nanocomposite solar cells have achieved greater than 5 % energy conversion efficiency under simulated AM 1.5 irradiation (AM: air mass).

In most chalcopyrite solar cells, a buffer layer is typically required between the n-type and p-type regions to control the interfacial properties. In the present 3D nanocomposite solar cells, a thin (ca. 30 nm) In_2S_3 buffer layer is applied between the TiO_2 and CIS layers. The buffer layer is particularly important for 3D nanocomposite solar cells because the large interfacial junction area increases the probability of recombination. The In_2S_3 buffer layer has previously been shown to dramatically improve the junction rectification and decreases recombination losses in TiO_2/CIS nanocomposite solar cells, thereby significantly increasing conversion efficiencies.[7]

In addition to controlling the interfacial properties, we have recently determined that careful control of the TiO_2 nanostructure—particularly the TiO_2 particle size and layer thickness—is critical in achieving good solar-cell performance. In this paper, the influence of the TiO_2 particle size is examined. Specifically, it is found that ultrasmall (9 nm) TiO_2 particles lead to poor solar-cell performance while larger particles (50–300 nm) lead to better performance. By employing current–voltage (*I–V*), impedance spectroscopy, and incident-photon-to-current conversion efficiency (IPCE) measurements, and photocurrent/photovoltage transient measurements, as well as physical sample characterization methods, the relationship between TiO_2 particle size and solar-cell performance is analyzed. As a result of this investigation, it is shown that larger TiO_2 particles lead to better photovoltaic performance owing to greatly improved electron transport. The larger TiO_2 particles may also secondarily help improve performance owing to enhanced photon absorption and improved interfacial characteristics.

2. Physical Characterization

The fabrication of TiO_2/CIS nanocomposite solar cells is described in detail elsewhere.[8] For more information, also consult the Experimental section at the end of this paper. To

[*] Dr. R. O'Hayre, M. Nanu, Prof. J. Schoonman, Prof. A. Goossens
Delft Institute for Sustainable Energy, Delft University of Technology
2628 BL Delft (The Netherlands)
E-mail: rohayre@stanford.edu
Dr. Q. Wang, Prof. M. Grätzel
Laboratoire de Photonique et Interfaces
Ecole Polytechnique Fédérale
1015 Lausanne (Switzerland)

[**] This material is based upon research supported by the National Science Foundation under Grant No. 0401817. Optical absorption measurements were acquired with the generous assistance of Ir. Annemarie Huijser, Optoelectronic Materials Section, Faculty of Applied Sciences, TU Delft.

ensure comparability, the 9, 50, and 300 nm samples were all processed at the same time, as a single batch. Therefore, they should only differ in the microstructure of the nanocrystalline TiO_2 layer. The Raman and X-ray diffraction (XRD) spectra presented in Figures 1 and 2, respectively, verify that the chemical composition and CIS quality are similar for all three samples. The broad Raman peak centered at 295 cm^{-1} indicates the presence of Cu–Au ordering (this peak is actually a doublet composed of the symmetric CIS peak at 290 cm^{-1} and the Cu–Au peak at 305 cm^{-1}).[9,10] Cu–Au ordering is undesirable, as it has been linked to sub-bandgap states and decreased photovoltaic performance, but it is frequently observed in spray-deposited CIS films.[11] As the XRD scan detail (Fig. 2 inset) indicates, there is some evidence for broadening of the anatase 200 peak with decreasing crystallite size. However, the resolution is insufficient to enable a reliable determination of crystallite size for the three samples. Furthermore, peak-broadening effects due to the nanocrystalline TiO_2 may be obscured by the signal from the dense TiO_2 underlayer.

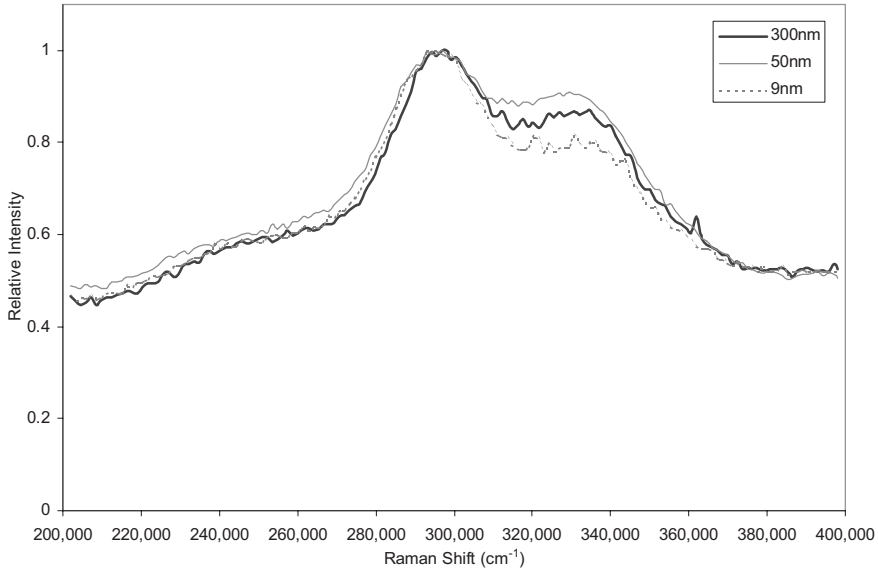

Figure 1. Raman spectra of the 9, 50, and 300 nm TiO_2/In_2S_3/CIS nanocomposite solar-cell samples. Nearly identical CIS peaks are observed for all three samples at 295 cm^{-1}.

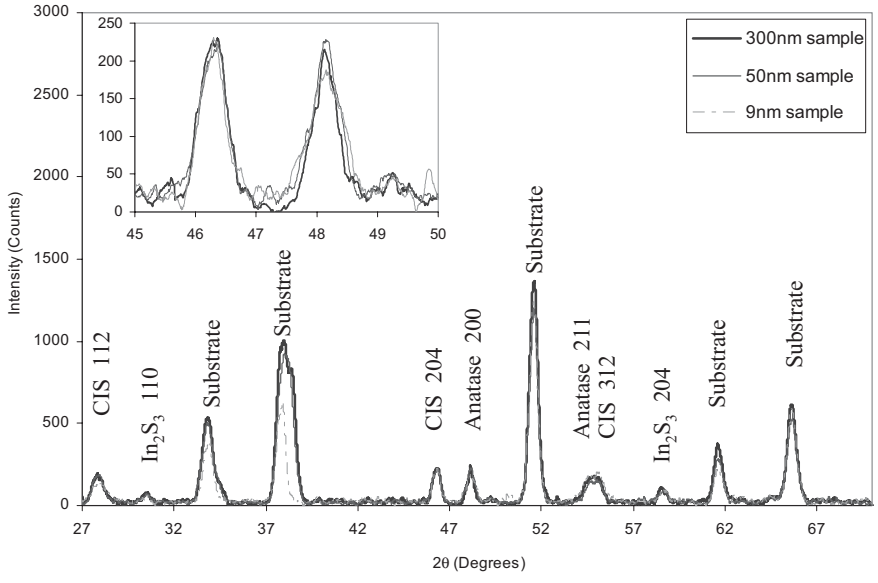

Figure 2. X-ray powder (2θ) diffraction patterns of the 9, 50, and 300 nm TiO_2/In_2S_3/CIS nanocomposite solar-cell samples. The patterns are nearly identical for all three samples, although minor differences can be observed in the inset scan of the anatase 200 peak.

3. Results and Discussion

3.1. *I–V* Response

Figure 3 presents typical *I–V* responses for the 9, 50, and 300 nm samples in the dark (Fig. 3a) and in the light (Fig. 3b). Table 1 summarizes the relevant solar-cell parameters for the three samples. As can be seen from these data, solar-cell performance increased significantly with increasing TiO_2 particle size. Efficiency increased from 0.2 % for the 9 nm sample to 2.8 % for the 300 nm sample due to improvements in open-circuit voltage (V_{oc}), short-circuit current (J_{sc}), and fill factor (*FF*). Compared to the 300 and 50 nm samples, the 9 nm sample showed poor rectifying characteristics, especially as illustrated by its *I–V* response in the dark. Compared to the 300 nm sample, the 50 and 9 nm samples showed much lower J_{sc}. The combination of improved junction rectification and improved J_{sc} greatly boosted the efficiency of the 300 nm sample as compared to the other two samples. In all samples, forward diode currents increased significantly under illumination compared to the dark, a commonly observed effect that is attributed to photodoping of the TiO_2.[12,13]

The *I–V* characteristics of the three cells may be further analyzed using a modified diode-equation approach that takes into account both series resistance (R) and G (G) losses[14]

$$J = J_o \exp\left[\frac{q}{AkT}(V - RJ)\right] + GV - J_L \quad (1)$$

In this equation, A is the diode ideality factor, q is the electron charge, k is Boltzmann's constant, T is temperature, J_L is the light current, and J_o is the exchange

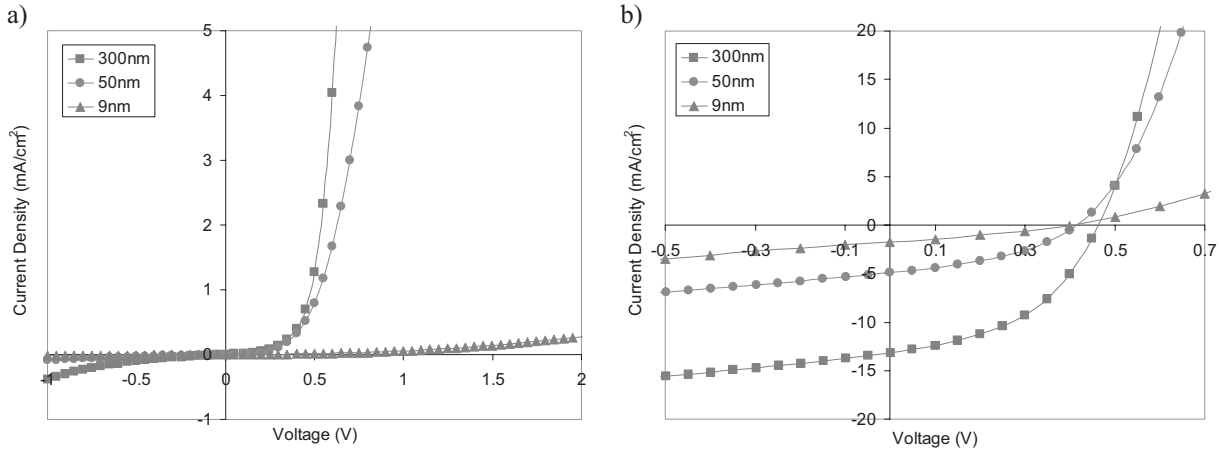

Figure 3. *I–V* curves in the dark (a) and under AM 1.5 simulated irradiation (b) for the 9, 50, and 300 nm TiO_2/In_2S_3/CIS nanocomposite solar cells. Solar-cell performance characteristics extracted from these *I–V* curves are summarized in Table 1. Parameters obtained from more detailed *I–V* curve analyses are provided in Table 2.

Table 1. *I–V* performance characteristics of the 9, 50, and 300 nm solar cells.

Sample	J_{sc} [mA/cm^2]	V_{oc} [V]	Fill factor	Efficiency [%]	J_{dark}[1.0V]/ J_{dark}[-1.0V]
9nm	1.72	0.405	0.30	0.21	2.73
50nm	4.91	0.405	0.41	0.81	99.7
300nm	13.2	0.460	0.46	2.80	68.6

current. Applying Equation 1 to the *I–A* curves presented in Figure 3 permits values for R, G, A, and J_o to be extracted for all three solar cells both in the dark and under illumination. The results of this analysis are presented in Table 2.

Table 2. *I–V* analysis summary of the 9, 50, and 300 nm solar-cell samples.

Sample	G [mS/cm^2]	R [Ωcm^2]	A	J_o [mA/cm^2]
300nm Dark	0.3	5.5	2.9	2.30E-03
300nm Light	5.1	2.6	3.7	6.62E-02
50nm Dark	0.19	5.5	3.6	6.70E-03
50nm Light	4	3.4	3.8	4.82E-02
9nm Dark	0.015	680	4.3	3.00E-04
9nm Light	3.3	83	3.45	3.70E-03

For good solar-cell performance, it is desirable to reduce G and R as much as possible. As Table 2 reveals, the 9 nm solar cell showed the lowest G and J_o values, indicating that this cell displays decreased shunts compared to the 50 and 300 nm cells. However, the 9 nm cell showed significantly larger R values compared to the 50 and 300 nm cells, confirming the higher transport resistance presented by this cell. In all cells, G increases and R decreases upon exposure to light. As mentioned previously, this is typical of photodoping behavior. For a well-behaved diode, the diode ideality constant A should vary between one and two. All three analyzed cells, however, showed a diode ideality factor greater than two, indicating decreased rectification compared to a well-behaved diode. Rectification was generally slightly improved in the 300 and 50 nm cells compared with the 9 nm cell.

In order to further confirm the hypothesis that the nanocrystalline TiO_2 matrix dominates the cell resistance, and hence the performance of the three solar-cell devices, blank TiO_2 cells were prepared and analyzed in a similar manner to the complete solar-cell devices. The blank cells were fabricated without In_2S_3 and CIS, and therefore contained only the dense and nanoporous TiO_2 layers. Figure 4 provides the *I–V* response from a 9 and a 300 nm blank sample. For both samples, the dense TiO_2 layer was approximately 100 nm thick and the nanoporous TiO_2 layer was approximately 350 nm thick. Al-

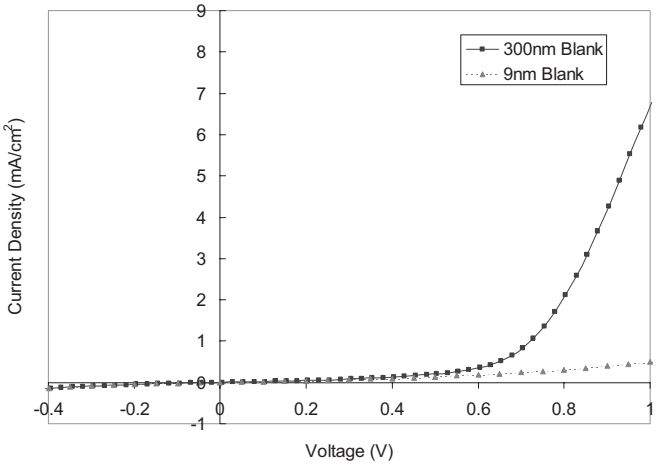

Figure 4. *I–V* curves in the dark for blank cells employing a 350 nm layer of either 9 nm TiO_2 crystallites or 300 nm TiO_2 crystallites. Although the film thickness is the same for both samples, the film fabricated from 9 nm crystallites shows significantly higher resistance. Parameters obtained from detailed analysis of these *I–V* curves are provided in Table 3.

ADVANCED FUNCTIONAL MATERIALS

though both blank samples had the same thickness, the sample prepared from the 9 nm TiO_2 particles clearly showed higher resistance. Table 3 provides results of the *I–V* analysis, confirming the dramatically larger series resistance presented by the 9 nm crystallite film.

Table 3. *I–V* analysis summary of the 9 and 300 nm blank samples.

Sample	G [mS/cm^2]	R [Ωcm^2]	A	J_o [mA/cm^2]
300nm (Blank) Dark	0.1	15.2	2.8	2.00E-05
9nm (Blank) Dark	0.15	583	3.9	4.70E-03

Compared to the complete solar-cell samples, the 300 nm blank sample showed increased dark R and decreased dark G, while the 9 nm blank showed decreased dark R and increased dark G. Furthermore, the dark J_o value for the 300 nm blank sample was considerably smaller than for the complete 300 nm solar-cell device. These differences can perhaps be explained by differences in interfacial area between the blank and complete solar-cell samples. CIS infiltration into the 300 nm solar-cell sample increases the interfacial contact area compared to the blank sample (see Fig. 5a). This infiltration likely leads to the increased G, increased J_o, and lowered R of the complete 300 nm solar-cell device. In contrast, CIS infiltration is not achieved in the 9 nm solar cell sample (see Fig. 5b). Thus, the thicker film used in the complete solar cell compared to the blank leads to increased R and decreased G.

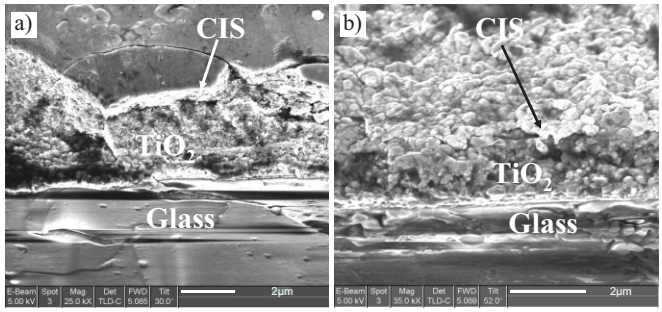

Figure 5. SEM cross-section images of the 9 nm (a) and 300 nm (b) solar-cell samples. The 300 nm sample shows a more intimate infiltration of the CIS overlayer into the nanoporous TiO_2 matrix.

IPCE profiles for the 9 and 300 nm samples are compared in Figure 7. Clearly, the 9 nm sample exhibits a severe reduction in the IPCE over the active wavelength range (from about 400 to 950 nm) compared to the 300 nm sample. As indicated by the *I–V* analysis, most of the IPCE decrease for the 9 nm sample must be attributed to ineffective charge-carrier collection, although a minor fraction of the IPCE decrease can also be attributed to the reduced absorption. Interestingly, the 300 nm sample absorbs strongly out to 950 nm, although the bandgap of CIS ($Eg = 1.5$ eV[15]) would suggest an IPCE cut-off at around 850 nm. The IPCE signal between 850 and 1000 nm is indicative of sub-bandgap states in the CIS absorber. These states have been observed previously in other studies.[16,17]

3.2. Optical Absorption and IPCE

The improved CIS infiltration and resulting interfacial area enhancement provided by the larger TiO_2 particle matrix also leads to improved optical absorption, as shown in Figure 6. This trend is likely due to the improved CIS infiltration as well as to increased light-scattering effects with increasing TiO_2 particle size. Profilometry measurements showed that the average surface corrugations increased from 150 nm for the 9 nm sample to 660 nm for the 300 nm sample; these increased surface corrugations may improve the light trapping. In addition to improved light collection, a more-intimate intermixing between the CIS and TiO_2 films reduces the average minority-carrier-migration pathway, thus improving the IPCE. While these effects may be minor compared to the change in charge-transport resistance, they certainly contribute to the improved performance of the larger-particle-size samples.

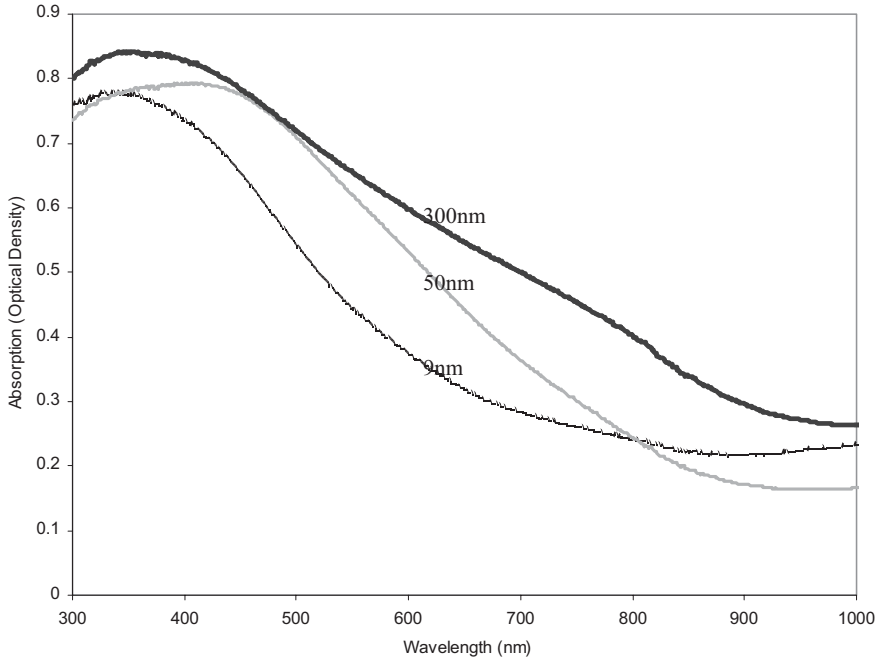

Figure 6. Absorption spectra from the 9, 50, and 300 nm solar cells. Optical density (OD = –log[transmittance]) increases at most wavelengths with increasing TiO_2 particle size.

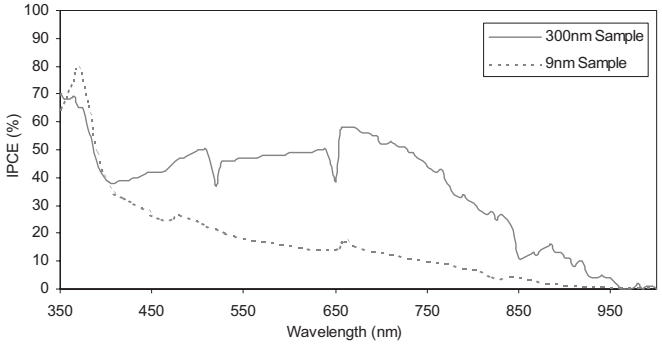

Figure 7. IPCE spectra from the 9 nm and 300 nm solar cells. IPCE is much higher in the 300 nm sample compared to the 9 nm sample, especially in the wavelength range corresponding to strong CIS absorption (450 to 850 nm).

3.3. Impedance in the Dark

To further study the charge-transport and rectification differences between the solar-cell samples, temperature-resolved impedance measurements were conducted. Figure 8 presents representative impedance spectra for the 9, 50, and 300 nm solar cells acquired at 275 K and 0 V bias in the dark. At all bias and temperature conditions, we find that the impedance data can be fitted to either a single or double RC (resistor–capacitor) equivalent circuit model. Figure 8 includes double RC model fits to the impedance spectra. At reverse bias and small forward bias, the complete double RC model is needed, although the impedance response is strongly dominated by the larger of the two RC elements. At high forward bias (typically beyond +0.6 V), only the single dominant RC element is needed. The complete equivalent circuit model is provided in the Figure 8 inset. In this circuit, R_{maj} and CPE_{maj} (*CPE*: constant-phase element) designate the dominant RC element, R_{min} and CPE_{min} designate the minor RC element, and R_s represents the series resistance element. Because the minor RC element is only relevant for a small potential range and typically accounts for less than 15 % of the total impedance signal, it is difficult to draw definite conclusions as to its physical significance. In this paper, therefore, our analysis is constrained to the major RC element.

Typically, we find that *CPE*s rather than simple capacitors are required for accurate fitting. The impedance of a *CPE* element is described by the following equation:

$$Z_{CPE} = \frac{1}{Q^{\circ}(j\omega)^{a}} \quad (2)$$

We interpret the *CPE* element as reflecting the 3D nature of the CIS/In_2S_3/TiO_2 structure. The 3D nanostructure inevitably leads to current inhomogeneities and therefore to the *CPE* response. The a values of the *CPE*s in the present fits typically range from 0.75 to 0.95, which are in the appropriate range for the distributed capacitance interpretation of the *CPE*. In our analysis, we do not attempt to convert the "Q°" value (Q° reflects an effective capacitance) of the *CPE* into a "true capacitance". Instead, we report *CPE* Q° values directly, yielding the unconventional units of $s^{-a}\,\Omega^{-1}$. If desired, the model of Hsu and Mansfeld[18] can be used to convert *CPE* Q° values into true capacitance values (with units of Farads). This method changes the absolute value, but not the trend of the reported data.

By nonlinear least-squares fitting the impedance spectra of the 9, 50, and 300 nm samples as a function of bias and temperature, values for R_s, R_{maj}, CPE_{maj}, R_{min}, and CPE_{min} were obtained. The sheet resistance of the transparent conducting oxide (TCO) glass primarily determines R_s. For all samples, R_s varied between 0.4 and 0.5 Ωcm^2 and was observed to be slightly temperature dependent but bias independent. In contrast, both R_{maj} and CPE_{maj} showed a strong bias dependence. Figure 9 presents the temperature and bias dependences of the fitted R_{maj} and CPE_{maj} values for the 300 nm sample. Figure 10 presents the corresponding R_{maj} and CPE_{maj} trends for the 9 nm sample. Equivalent circuit-element values for the 50 nm sample have also been extracted, but are not shown, since they closely resemble the data for the 300 nm sample. Since the dark *I–V* curves for the 300 and 50 nm samples are similar, it is reassuring that they show similar dark impedance behavior. In Figures 9 and 10, the impedance versus bias response of the 300 and 9 nm samples is presented for a series of temperatures from 200 to 350 K. The temperature data reveal that R_{maj} is strongly temperature dependent, while CPE_{maj} is essentially temperature independent. The temperature dependence will be discussed in further detail later in this section.

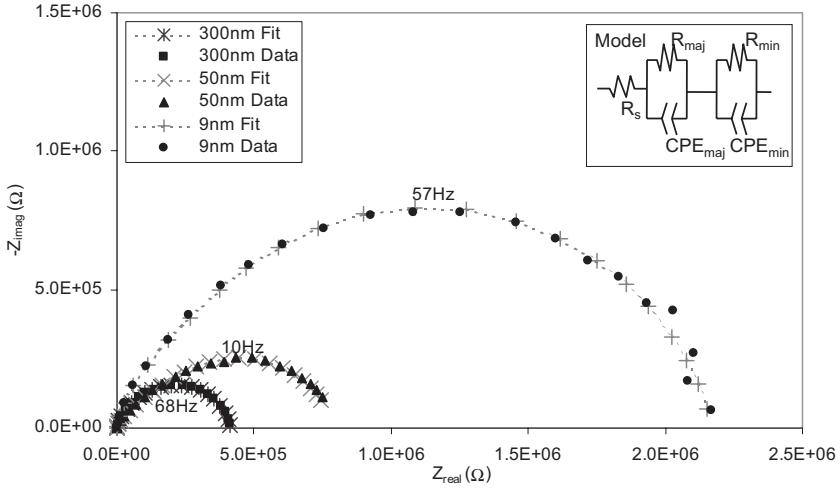

Figure 8. Representative Nyquist impedance spectra (and corresponding model fits) of the 9, 50, and 300 nm solar cells. All three spectra were acquired at 275 K and 0 V bias in the dark. All three impedance spectra are well fit by the double *R–CPE* equivalent circuit model shown in the figure inset.

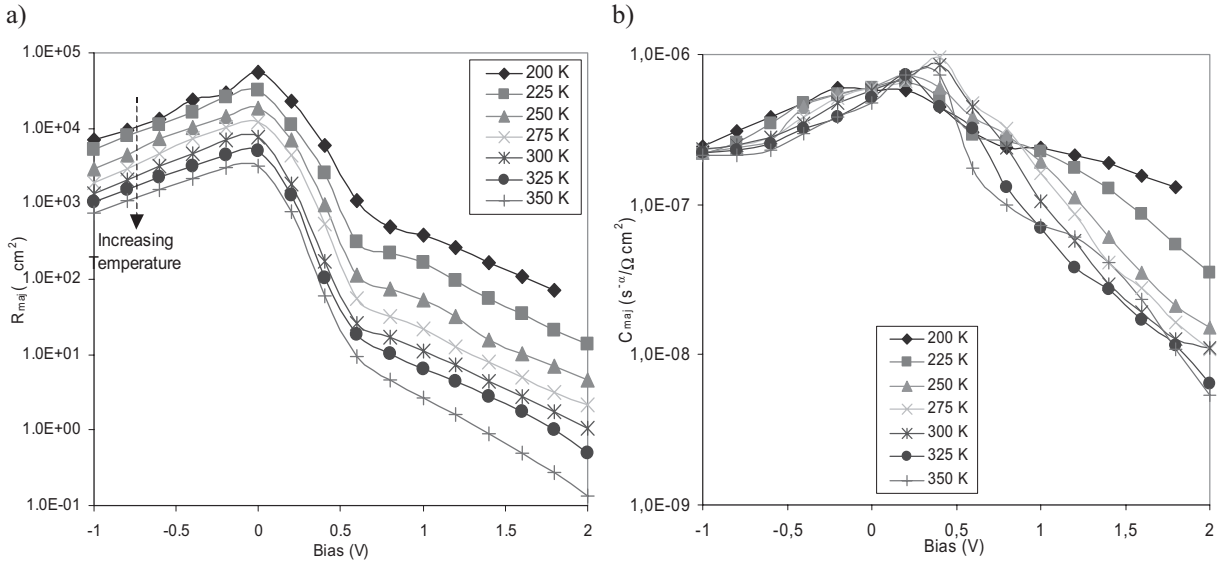

Figure 9. R_{maj} (a) and CPE_{maj} (b) as a function of applied bias and temperature for the 300 nm solar cell.

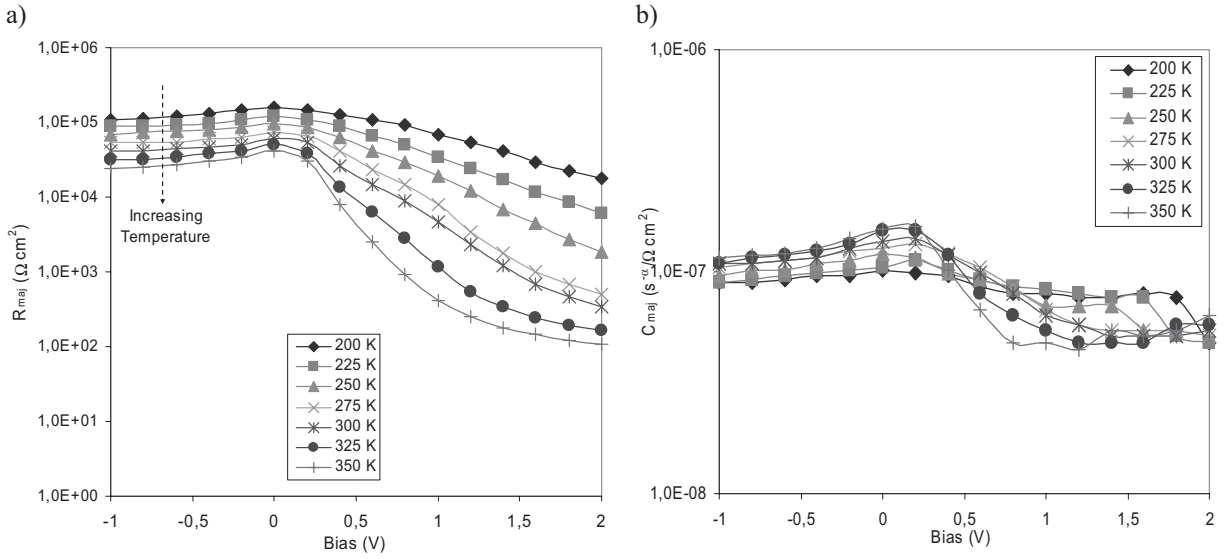

Figure 10. R_{maj} (a) and CPE_{maj} (b) as a function of applied bias and temperature for the 9 nm solar cell.

In Figure 9a, R_{maj} shows three distinct regions of behavior versus bias: 1) reverse bias ($V<0$), 2) small forward bias ($0<V<0.5$ V), and 3) large forward bias ($V>0.5$). In reverse bias, R_{maj} decreases gradually with increasing negative bias. For an ideal diode, the cell impedance approaches infinity in the reverse-bias condition. In the standard leakage model of a diode, the reverse-bias leakage current is modeled by a finite but constant resistance in the reverse-bias regime. The impedance data, however, reveal a bias-dependant leakage resistance. This bias-dependant leakage resistance may be caused by electron injection from the valance band of CIS into the conduction band of TiO_2 via trap states in the In_2S_3 buffer layer. Ongoing studies indicate that increasing the In_2S_3 buffer layer thickness commensurately decreases the reverse-bias leakage current, supporting this hypothesis.[19] In the reverse-bias regime, the leakage current is much larger than the diode current, and therefore R_{maj} extracted from the impedance measurements should be comparable to the dark G value calculated from I–V analysis (for $R_{maj} \gg R_s$). Although the I–V analysis assumed a bias-independent G, while R_{maj} is clearly bias-dependant, at reasonable reverse bias voltages the correspondence between R_{maj} and G is strong. For example, at $V=-0.50$ V and $T=300$ K, $R_{maj} \approx 3500\ \Omega cm^2$, which converts to a G value of 0.29 mS cm^{-2}. This corresponds almost exactly with the G value of 0.30 mS cm^{-2} extracted from the room-temperature I–V analysis of the 300 nm solar cell in the dark.

In the small-forward-bias condition, R_{maj} decreases strongly with increasing bias. In this region, R_{maj} reflects the diode resistance of the p–n junction. This diode resistance decreases exponentially with increasing forward bias. From the slope of the curve in this regime, A can be extracted. The value of A varies from approximately 3.7 to 5.4, and decreases with increasing temperature. The A values determined from this impedance analysis are higher than those determined from the previous I–V analysis. This is probably because R_{maj} from the impedance data cannot be directly compared to the series resistance and G-corrected I–V data (especially since R_{min} is neglected).

In the high-forward-bias regime ($V > 0.5$ V), R_{maj} decreases much more slowly with increasing bias. In this high-forward-bias regime the system is likely above the flat-band potential of the CIS/In_2S_3 junction. (This interpretation is substantiated by the V_{oc} voltage values of approximately +0.4 V for the cells under irradiation.) Above flat band, the diode impedance of the p–n junction no longer dominates the impedance response of the cell. Instead, we propose that percolating electron transport in the nanostructured TiO_2 dominates the cell impedance. Since the diode is effectively shorted in this regime, the sum of the impedance elements ($R_{maj} + R_s$) should approach the value of the series resistance, R, computed from the dark I–V curve analysis of the 300 nm solar cell. Over the voltage range 0.60–2.0 V, ($R_{maj} + R_s$) varies from approximately 1.0–10.0 Ωcm^2, bracketing the fixed I–V analysis value of $R = 5.5$ Ωcm^2.

While the I–V analysis assumed a bias-independent series resistance, R_{maj} is observed to decrease slowly with increasing bias in this high-bias regime. This behavior likely reflects the bias-dependent passivation of surface or bulk trap states in the TiO_2 nanoparticles. Electronic transport in TiO_2, a wide-band-gap semiconductor, is often described with trap-based models. An exponential distribution of trap energies can be modeled as[20]

$$N_t(E) = N_o e^{(E-E_c)/kT_t} = N_n e^{(E-F)/kT_t} \quad (3)$$

where $N_t(E)$ is the energetic distribution of the traps, E_c is the conduction-band energy, T_t is an effective temperature parameter describing the width of the trap distribution, F is the Fermi level, and N_n is given by

$$N_n = N_o e^{(F-E_c)/kT_t} \quad (4)$$

Integrating Equation 3 over energy allows the concentration of traps, n_t that are filled at a given F to be calculated:

$$n_t = kT_t N_o e^{(F-E_c)/kT_t} \quad (5)$$

As more traps are filled, the resistivity, ρ, should decrease, because fewer empty traps remain to stall conduction-band electrons. Assuming that the resistivity is inversely proportional to the concentration of filled traps, we can write

$$\rho = \frac{B}{n_t} = BkT_t N_o e^{-(F-E_c)/kT_t}$$
$$= BkT_t N_o e^{-(F_o-E_c)/kT_t} e^{-qV/kT_t} \quad (6)$$

where B is a constant and we have used the fact that $F = F_o + qV$, where F_o is the Fermi level at zero volts bias and V is the applied bias. Grouping all the bias-independent terms into a single constant, ρ_o, allows the bias dependence of the resistivity to be expressed in the final simplified form:

$$\rho = \rho_o e^{-qV/kT_t} \quad (7)$$

where q is the electron charge. From the impedance data in the high-forward-bias regime, R_{maj} may be fit to this trap-passivation resistivity model, allowing both ρ_o and the characteristic trap width to be determined. While ρ_o is strongly temperature dependent (which will be discussed later), the trap distribution is fairly temperature insensitive and varies from $kT_t = 0.52$ eV at $T = 200$ K to $kT_t = 0.42$ eV at $T = 350$ K. This trap-distribution width is reasonable for TiO_2, which has an energy gap of approximately 3.6 eV.

Figure 9b presents the variation of CPE_{maj} with bias for the 300 nm sample. If it is interpreted as a capacitance, the value for CPE_{maj} is consistent with a junction or interfacial capacitance. Using the parallel-plate capacitor equation

$$\frac{C}{A} = \frac{\varepsilon_o \varepsilon}{d} \quad (8)$$

where C is capacitance, A is the area, ε_o is the permittivity of free space, and ε is the dielectric constant, provides an estimate for the "effective" thickness, d, of the junction. Inserting $C/A = 5 \times 10^{-7}$ F cm^{-2} and assuming $\varepsilon = 11$ (a reasonable estimate for CIS) yields $d = 19$ nm. CPE_{maj} is observed to increase with increasing bias up to about +0.4 V, and then to decrease at higher bias. Like the slope change observed for the R_{maj} curves, the CPE_{maj} maximum coincides roughly with the onset of the flat-band potential. Below the flat band, the CPE_{maj} response shows typical Mott–Schottky behavior, indicating space-charge-layer formation. Experiments are currently ongoing to further discern the location and nature of the space-charge region in these nanocomposite samples.[19] Above the flat band CPE_{maj} decreases with increasing bias. Above the flat band, we propose that the p–n junction no longer dominates the transport dynamics of the system; instead, electron transport in the TiO_2 nanostructure dominates the impedance response and the decreasing capacitance likely reflects the increasingly ohmic nature of charge transport in the TiO_2 nanostructure and the passivation of trap states.

Figure 10a presents the variation of R_{maj} with bias for the 9 nm sample. In contrast to the 300 nm sample, R_{maj} for the 9 nm sample shows a far less distinct separation into three regimes. A strong p–n junction diode response is only seen at the highest temperatures. At lower temperatures, we hypothesize that percolating electron transport in the 9 nm TiO_2 nanostructure is the major bottleneck, strongly influencing the impedance response at all bias voltages. At low temperatures (200–250 K) or at high temperature and high bias voltage ($T > 325$ K, $V > 1.0$ V), the variation of R_{maj} can be described as before using the trap-passivation resistivity model. Again, ρ_o is highly temperature sensitive, while the trap-distribution width varies from $kT_t = 0.77$ eV at $T = 200$ K to $kT_t = 0.43$ eV at $T = 350$ K. Similar trap distributions are obtained from both the 9 and 300 nm samples, indicating that the physical character of the traps in both samples are likely to be the same even though the absolute number of traps (and therefore the size of ρ_o) is considerably larger in the 9 nm sample compared to the 300 nm sample.

The number of traps in the 9 nm TiO_2 nanostructure is likely to be much greater than for the 300 nm structure because of the greatly increased surface-to-volume ratio (assuming surface traps dominate) and the greatly increased number of interparticle impediments. A 1.5 μm thick TiO_2 film composed of 300 nm particles presents on the order of 10 particle–particle junctions, whereas the same film composed of 9 nm particles would present on the order of 300 particle–particle junctions. The increase in particle–particle junctions in the 9 nm sample compared to the 300 nm sample is accompanied by a commensurate increase in the magnitude of the R_{maj} element (compare Figs. 8a and 9a). At 0 V bias, R_{maj} for the 9 nm sample was approximately 10 times larger than R_{maj} for the 300 nm sample. At 1 V bias, R_{maj} for the 9 nm sample was 100 times larger than R_{maj} for the 300 nm sample. This difference is also reflected in the *I–V* analysis results, which also showed approximately 10 times larger resistance in the 9 nm sample compared to the 300 nm sample ($R = 5.5$ Ωcm^2 versus $R = 683$ Ωcm^2). The agreement between the *I–V* and impedance data therefore reinforces the hypothesis that highly resistive electron transport in the 9 nm sample severely limits charge-carrier collection.

Figure 10b presents the variation of CPE_{maj} with bias for the 9 nm sample. Like the 300 nm sample, the 9 nm sample showed a maximum in CPE_{maj}. This maximum occurred at around 0.2 V. As with the 300 nm sample, space-charge formation is observed for $V < 0.20$ V. In contrast to the 300 nm sample, CPE_{maj} did not decrease as strongly with increasing forward bias. At reverse bias and small forward bias, the CPE_{maj} values measured for the 9 nm sample were approximately 2–4 times smaller than those for the 300 nm sample. The smaller capacitance of the 9 nm sample likely reflects the smaller roughness and smaller interfacial area of the TiO_2/In_2S_3/CIS junction in the 9 nm sample compared to the 300 nm sample. This hypothesis is supported by the scanning electron microscopy (SEM) images in Figure 5 as well as by the profilometry measurements of sample surface corrugations. (As noted earlier, the surface corrugations in the 300 nm sample are approximately four times larger than in the 9 nm sample.) At high forward bias, the CPE_{maj} values for the 9 nm sample are greater than those for the 300 nm sample. In the high-forward-bias region, where electron transport through the TiO_2 nanostructure dominates the impedance response of the samples, the higher capacitance likely reflects the larger number of trap states and interparticle junctions present in the 9 nm TiO_2 network compared to the 300 nm TiO_2 network. In other words, the high-bias capacitance originates not from the TiO_2/In_2S_3/CIS interface, which is shorted at high bias, but from the TiO_2 particle network. At high bias voltages, CPE_{maj} for the 9 nm sample is 10–100 times larger than CPE_{maj} for the 300 nm sample, mirroring the trend in R_{maj} and consistent with the 30-fold increase of interparticle junctions presented by the smaller grain-sized material.

Figure 11a and b presents the temperature dependence of R_{maj} for the 300 nm and 9 nm samples, respectively, at several

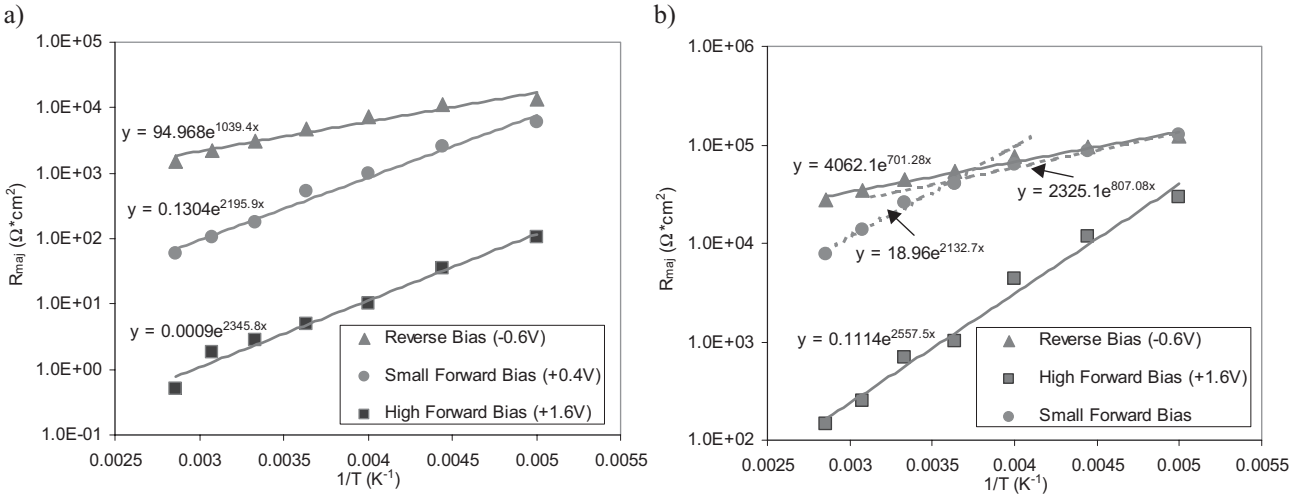

Figure 11. Arrehenius plots of R_{maj} for the 300 nm sample (a) and the 9 nm sample (b) at three different applied voltages. Arrehenius-type activated behavior is seen in both samples. Activation energies extracted from the plots are summarized in Table 4.

different bias voltages. In both samples, R_{maj} exhibits Arrhenius-type temperature-activated behavior. The activation energies extracted from these figures are summarized in Table 4. The relatively small temperature activation exhibited in reverse bias is consistent with the interpretation of leakage caused by charge injection across the p–n junction. This leakage process should not be highly temperature dependent. At high forward bias, the activation energy of around 0.2 eV observed for both the 300 and 9 nm samples may be associated with the average depth of conduction-band-edge trap-states in the nanostructured TiO_2. The correlation between these activation-energy values and the previously determined trap-state distributions reinforces this hypothesis. The similar activation-energy values obtained from both the 9 and 300 nm samples at high forward bias, like the similarity in trap-distribution widths again indicates that the physical mechanisms governing the charge-transport process are likely the same in both samples. Previous studies of electron transport in nanostructured TiO_2 report activation energies in the same range as we report here.[21–23] Interestingly, in the small-forward-bias regime, the 9 nm sample shows a change in activation energy with increasing temperature. At high temperatures, the activation energy is similar to the high-forward-bias case. At low temperatures, however, the activation energy mirrors the reverse bias case.

Table 4. Activation energies extracted from Figure 11 for the 300 and 9 nm samples.

Sample	E_a [eV] at reverse bias (-0.6V)	E_a [eV] at small forward bias (0.4V)	E_a [eV] at high forward bias (1.6V)
9nm	0.061	0.069 (T < 275K) 0.184 (T > 275K)	0.220
300nm	0.090	0.189	0.202

3.4. Impedance under Illumination

Room-temperature impedance measurements under illumination (simulated AM 1.5) were obtained for the 9 and 300 nm samples as a function of bias from short circuit to V_{oc}. For both samples, the single *R–CPE* equivalent circuit model was found to satisfactorily fit the measured impedance spectra at all bias values. The *R* and *CPE* values extracted from the fits are summarized in Figure 12. As Figure 12a shows, for both the 9 and 300 nm samples the resistance under illumination is much smaller than the resistance measured in the dark (compare Figs. 9a and 10a), mirroring the previously analyzed *I–V* curve behavior. This effect is also observed in dye-sensitized solar cells (DSSCs) and is attributed to photodoping at the interface, which increases charge-carrier concentrations and fills the trap states.[12,13] As Figure 12b shows, the *CPE* values under illumination have increased slightly (by a factor of approximately two or three) compared to their values in the dark. This effect is also observed in DSSCs and is again associated with photodoping.[24] While the 300 nm sample still shows a maximum in capacitance at small forward bias, the 9 nm sample shows a slight but monotonic decline in capacitance with increasing bias.

3.5. Photovoltage/Photocurrent Transients

Figure 13 presents photovoltage transient (Fig. 13a) and photocurrent transient (Fig. 13b) results for the 9 and 300 nm cells. Cell time constants range from 1 to 1.7 ms in all measurements, with the 300 nm cell showing slightly longer time constants, indicating longer charge-carrier lifetime than the 9 nm cell. However, because the measured transients approach the experimental resolution limits, significant error may be present in these data. Capacitance values calculated from the transient measurements indicate that the 300 nm solar cell possesses a much larger capacitance under operating conditions ($C = 2.5\ \mu F\,cm^{-2}$ for the 300 nm cell, $C = 0.14\ \mu F\,cm^{-2}$ for the 9 nm cell).

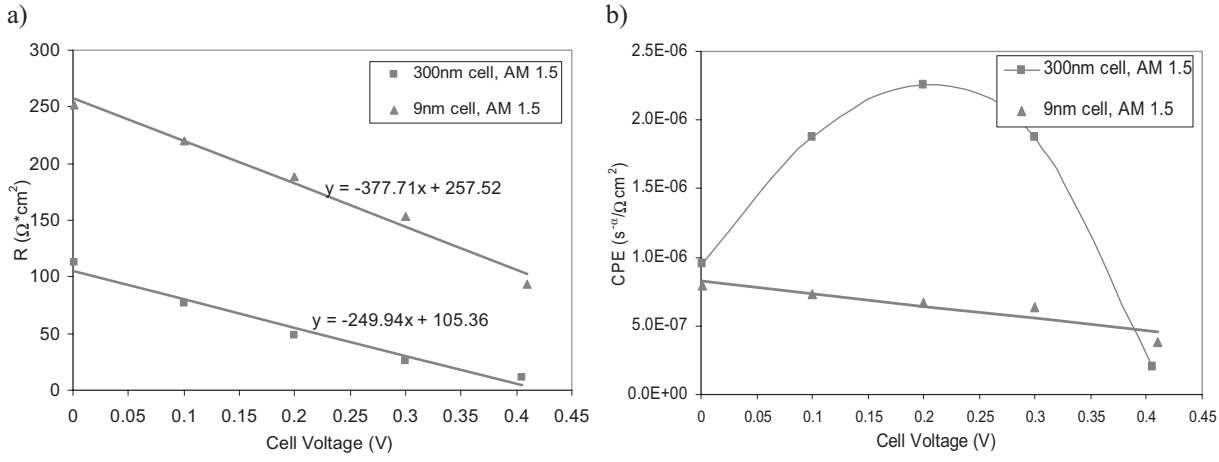

Figure 12. *R* (a) and *CPE* (b) as a function of bias for the 300 nm and 9 nm solar cells under simulated AM 1.5 irradiation. Compared to the situation in the dark, both cells show slighter higher capacitance and much lower resistance under illumination. (Compare with Figs. 9,10.)

ADVANCED FUNCTIONAL MATERIALS

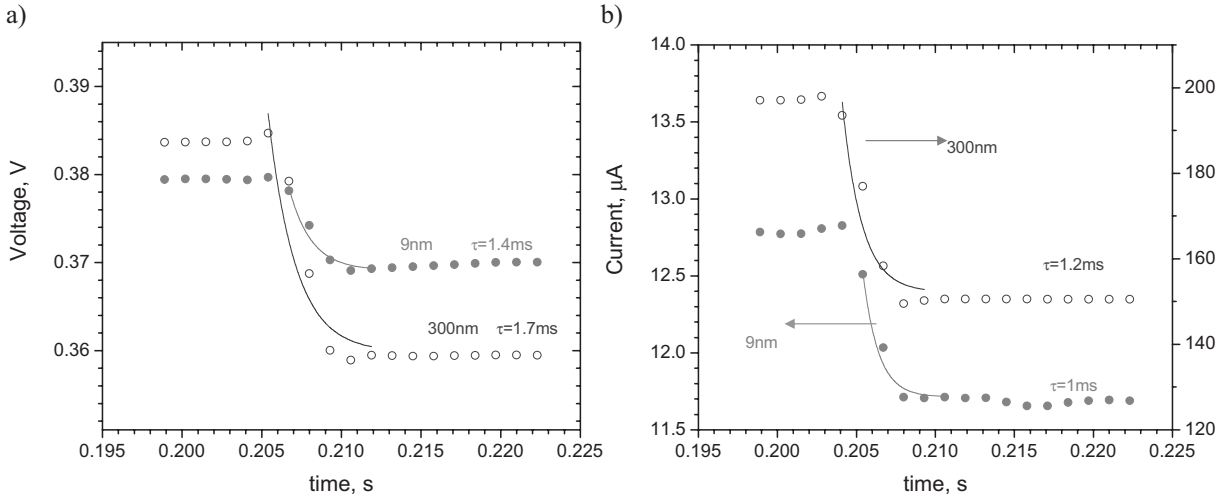

Figure 13. Photovoltage transients (a) and photocurrent transients (b) for the 300 nm and 9 nm cells.

Compared with liquid DSSCs, the TiO_2/In_2S_3/CIS nanocomposite cells display much-faster transient response. The photovoltage transients (measured at V_{oc}) indicate a faster recombination process compared to DSSCs, whereas the photocurrent transients (measured at short circuit) likely indicate a faster charge-collection process compared to DSSCs. However, because IPCE measurements show incomplete charge collection at short circuit, we cannot wholly attribute the photocurrent decay to a pure charge-collection process. The presence of charge recombination may also contribute to the photocurrent transient even in the short-circuit state and consequently the charge transport within the film may be overstated. The speed and similarity of the time constants for the photovoltage and photocurrent transients therefore indicates that charge recombination plays an especially critical role in determining the performance of TiO_2/In_2S_3/CIS nanocomposite solar cells.

4. Conclusions

We have observed that the performance of TiO_2/In_2S_3/CIS nanocomposite solar cells depends strongly on the underlying TiO_2 nanostructure. For a series of solar cells fabricated from 9, 50, and 300 nm TiO_2 nanoparticles, performance is observed to increase with increasing particle size. We hypothesize that the performance improvements are primarily due to significantly improved charge transport with increasing particle size. Both *I–V* curve analysis and impedance measurements in the dark imply that the 9 nm sample is severely limited by electron transport within the nanostructured TiO_2 layer at room temperature and below, obscuring the rectification behavior of the p–n junction. Even under illumination, the 9 nm sample suffers from a twofold larger resistance compared to the 300 nm sample, reducing the *FF* and thus harming photovoltaic performance. Although the 9 nm sample shows significantly higher charge-transport resistance compared to the 300 nm sample, they both display trap-dominated transport with similar trap-distribution widths and activation energies. The dramatic increase in the resistance of the 9 nm sample compared to the 300 nm sample therefore likely stems from an increase in the number of traps, rather than from a change in the underlying transport physics.

Further effects of increased TiO_2 particle size include increased absorption and decreased carrier-migration distance owing to enhanced light trapping and better infiltration of the CIS overlayer into the TiO_2 matrix.

Similar time constants are obtained from both photocurrent and photovoltage transient measurements in TiO_2/In_2S_3/CIS nanocomposite solar cells. This similarity, combined with the speed of the photovoltage transient decay, indicates that TiO_2/In_2S_3/CIS nanocomposite solar cells suffer from extremely fast charge-carrier recombination. Thus, recombination likely plays a crucial role in determining the overall performance of these cells.

Based on these observations, we formulate the following suggestions for optimizing TiO_2/In_2S_3/CIS nanocomposite solar cells: 1) Optimize electron transport and reduce recombination losses in the TiO_2 matrix by keeping the TiO_2 film thin (<1 μm) and employing relatively large (>50 nm) TiO_2 nanoparticles. 2) Provide a sufficiently open TiO_2 microstructure to ensure intimate infiltration of the In_2S_3 buffer and CIS overlayer into the TiO_2 matrix.

5. Experimental

The fabrication of TiO_2/CIS nanocomposite solar cells is briefly summarized below. First, a dense film of anatase TiO_2 (ca. 100 nm) was deposited onto a transparent conducting oxide (TCO, LOF Tec 10) glass substrate using chemical spray pyrolysis. Next, a nanocrystalline anatase-TiO_2 coating was applied using the doctor-blade technique (ca. 1 μm thick). Three different nanocrystalline films based on commercially available precursor pastes (Solaronix, Inc.) containing 9, 50, and 300 nm anatase TiO_2 crystallites, respectively, were prepared. We refer to these as the 9, 50, and 300 nm solar cell samples throughout this paper. After annealing at 450 °C for 6 h in air, the samples were

coated with a spray-deposited n-type In_2S_3 buffer layer (ca. 30 nm) followed by p-type $CuInS_2$ (ca. 1 μm) [25]. Finally, gold contacts are evaporated on top of the CIS to define test cells (0.0314 cm^2 in area). In all electrical measurements, the gold/CIS electrode served as the working electrode, while the TCO/TiO_2 electrode served as the counter/reference electrode. Thus in forward bias, the CIS layer was positive relative to the TiO_2 layer.

Optical transmission spectra were recorded with a Perkin Elmer Lambda 900 UV/VIS/NIR spectrometer, using an integrating sphere. *I–V* measurements were performed in the dark and under illumination using a Princeton Applied Research 273 potentiostat/galvanostat. AM 1.5 measurements were acquired using a calibrated solar simulator (Solar Constant 1200, K.H. Steuernagel Lichttechnik GmbH). Impedance measurements in the dark were acquired with a Solartron 1255 FRA in combination with a Princeton Applied Research 283 potentiostat/galvanostat. Impedance measurements under illumination were acquired at EPFL in Lausanne using an EG&G M273 potentiostat coupled to an EG&G M1025 frequency response analyzer under a bias illumination of 100 $mW\,cm^{-2}$ (AM 1.5, 1 sun) from a 450 W Xenon light source. All impedance measurements were conducted with a 10 mV sinusoidal excitation signal. IPCE measurements were acquired at EPFL by measuring the wavelength dependence of the IPCE using light from a 300 W Xenon lamp (ILC Technology, USA) focused onto the cell through a Gemini-180 double monochromator (Jobin Yvon Ltd., UK). The monochromator was incremented through the visible spectrum to generate the IPCE(λ) curve. Photovoltage/photocurrent transients were observed using a pump pulse generated by a ring of red light-emitting diodes (LEDs) controlled by a fast solid-state switch. Pulse widths of 100 μs were used, with a rise and fall time of ~2 μs. Visible-bias light was supplied by a white-LED matrix and attenuated when needed by neutral-density filters. The time resolution of the potentiostat is 20 μs; thus, transient phenomena with time constants >40 μs could be measured.

Because of the small electrode area used in these studies, *I–V* and IPCE measurements were performed both with and without a mask to determine if a significant spreading current contributed to the measured results. In all cases, the measurements with and without a mask differed by less than 5 %. For consistency, all results presented in this paper are for the mask-free measurements.

Received: September 21, 2005
Final version: December 11, 2006
Published online: June 27, 2006

[1] B. O'Regan, M. Grätzel, *Nature* **1991**, *353*, 737.
[2] Q. Pei, G. Yu, C. Zhang, Y. Yang, A. J. Heeger, *Science* **1995**, *270*, 719.
[3] E. W. McFarland, J. Tang, *Nature* **2003**, *421*, 616.
[4] U. Bach, D. Lupo, P. Comte, J. E. Moser, F. Weissörtel, J. Salbeck, H. Spreitzer, M. Grätzel, *Nature* **1998**, *395*, 583.
[5] P. Wang, S. M. Zakeeruddin, J. E. Moser, M. K. Nazeeruddin, T. Sekiguchi, M. Grätzel, *Nat. Mater.* **2003**, *2*, 402.
[6] M. Nanu, J. Schoonman, A. Goossens, *Adv. Mater.* **2004**, *16*, 453.
[7] F. Lenzmann, M. Nanu, O. Kijatkina, A. Belaidi, *Thin Solid Films* **2004**, *451*, 639.
[8] M. Nanu, J. Schoonman, A. Goossens, *Nano Lett.* **2005**, *5*, 1716.
[9] J. Alvarez-Garcia, A. Perez-Rodriguez, B. Barcones, A. Romano-Rodriguez, J. R. Morante, A. Janotti, S. H. Wei, R. Scheer, *Appl. Phys. Lett.* **2002**, *80*, 562.
[10] J. Alvarez-Garcia, A. Perez-Rodriguez, A. Romano-Rodriguez, A. Janotti, J. R. Morante, R. Scheer, W. Calvet, *Thin Solid Films* **2001**, *387*, 216.
[11] I. Oja, M. Nanu, A. Katerski, M. Krunks, A. Mere, J. Raudoja, A. Goossens, *Thin Solid Films* **2005**, *480*, 82.
[12] F. Fabregat-Santiago, J. Bisquert, G. Garcia-Belmonte, G. Boschloo, A. Hagfeldt, *Sol. Energy Mater. Sol. Cells* **2005**, *87*, 117.
[13] Q. Wang, J. E. Moser, M. Grätzel, *J. Phys. Chem. B* **2005**, *109*, 14 945.
[14] S. Hegedus, W. N. Shafarman, *Prog. Photovoltaics* **2004**, *12*, 155.
[15] D. C. Look, J. C. Manthuruthil, *J. Phys. Chem. Solids* **1976**, *37*, 173.
[16] K. S. Ramaiah, V. S. Raja, *J. Mater. Sci. Mater. Electron.* **1999**, *10*, 145.
[17] J. Klaer, J. Bruns, R. Henninger, *Inst. Phys. Conf. Ser.* **1998**, *152*, 963.
[18] C. S. Hsu, F. Mansfeld, *Corrosion* **2001**, *57*, 747.
[19] R. O'Hayre, unpublished.
[20] M. A. Lampert, P. Mark, in *Current Injection in Solids*, Academic, New York **1970**, Ch. 2, p. 26.
[21] H. Greijer-Angrell, G. Boschloo, A. Hagfeldt, *J. Phys. Chem. B* **2004**, *108*, 12 388.
[22] A. Goossens, B. Van der Zanden, J. Schoonman, *Chem. Phys. Lett.* **2000**, *331*, 1.
[23] G. Boschloo, A. Hagfeldt, *J. Phys. Chem. B* **2005**, *109*, 12 093.
[24] J. van de Lagemaat, N. G. Park, A. J. Frank, *J. Phys. Chem. B* **2000**, *104*, 2044.
[25] I. Oja, M. Nanu, A. Katerski, M. Krunks, A. Mere, J. Raudja, A. Goossens, *Thin Solid Films* **2005**, *480*, 82.